ARTICLE

The effect of cation size on structure and properties of Ba-based tetragonal tungsten bronzes $Ba_4M_2Nb_{10}O_{30}$ (M=Na, K or Rb) and $Ba_4M_2Nb_8Ti_2O_{30}$ (M=Ca or Sr).

Nora Statle Løndal [a], Benjamin Albert Dobson Williamson [a], Julian Walker [a], Mari-Ann Einarsrud [a] and Tor Grande*[a]

The second largest family of oxide ferroelectrics, after perovskites, are the tetragonal tungsten bronzes (TTB) with the general formula $A2_4A1_2C_4B1_2B2_8O_{30}$. Cation disorder in TTBs is known to occur if the size difference between cations is small, but the impact of cation disorder on structure and properties have not yet been extensively addressed. In this study we investigate the effect of the size of the M cation, including cation disorder, on the crystal structure and dielectric properties in the two series $Ba_4M_2Nb_{10}O_{30}$ (BMN, A = Na, K and Rb) and $Ba_4M_2Nb_8Ti_2O_{30}$ (BMNT, M = Ca, Sr). Dense and phase pure ceramics in the two series were prepared by a two-step solid state synthesis route. The crystal structures of the materials were characterized by powder X-ray diffraction combined with Rietveld refinement. A close to linear relation between the in-plane lattice parameter (a) and the size of the M-cation were observed. $Ba_4M_2Nb_8Ti_2O_{30}$ was shown to possess cation disorder on the A-sites in line with previous work on $Ba_4M_2Nb_{10}O_{30}$. Thermodynamic calculations from density functional theory also indicated a drive for cation disorder in the three BMN compositions. Non-ambient temperature X-ray diffraction revealed contraction of the in-plane (a) and expansion of the out-of-plane (c) lattice parameters at the ferroelectric phase transition for $Ba_4M_2Nb_{10}O_{30}$. The ferroelectric transition temperature acquired by dielectric spectroscopy showed a systematically increasing T_C with decreasing size of the M-cation within both compositional series studied. The compositional dependence of T_C is discussed with respect to the size of the M-cation, cation disorder and the tetragonality, as well as the Ti-content. The relaxor to ferroelectric properties observed by polarization-electric field hysteresis loops are discussed in relation to the relative size of cations on the on A1 and A2 sites and the Ti-content.

Introduction

Ferroelectric materials exhibit both spontaneous and switchable polarisation and piezoelectric response. These properties are useful in capacitors, sensors, actuators, and transducers, which are key components in devices essential to our society such as smart phones, medical ultrasound and sonars.[1] The second largest family of conventional oxide ferroelectrics after perovskites are the tetragonal tungsten bronzes (TTBs).[2] The TTB structure, as seen in Figure 1, is more complex than the perovskite structure and possesses a total of five distinct cation sites.. This provides large chemical flexibility and a wide potential to customise ferroelectric properties within the structural framework of TTBs.

The general TTB formula is $A2_4A1_2C_4B1_2B2_8O_{30}$ and consist of a network of corner sharing BO_6-octahedra.[2] Generally, small and highly charged cations, such as Nb^{5+} and Ti^{4+}, are located in the octahedral B-sites.[3] The octahedra are organized in such a

way that four pentagonal, two square and four trigonal channels run through the structure parallel to the c-axis. These three types of channels make up the A2-, A1- and C-sites, respectively. When viewed along the c-axis, each octahedron is adjacent to four channels, two of which are pentagonal. The two different octahedral cation sites are labelled B1 or B2. With various cation combinations and stoichiometries the TTB framework can be described as "unfilled", "filled" or "stuffed", referring to whether some A-sites are unoccupied, all A-sites are occupied, or both A- and C-sites are fully occupied, respectively.[4] The occupational ordering of cations in the two A-
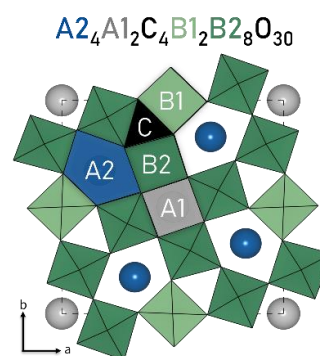
$$A2_4A1_2C_4B1_2B2_8O_{30}$$

Figure 1. Schematic of the Tetragonal Tungsten Bronze structure, as seen in the ab-plane.

[a.] Department of Materials Science and Engineering, NTNU Norwegian University of Science and Technology, NO-7491 Trondheim, Norway.
*Author to whom correspondence should be addressed. e-mail tor.grande@ntnu.no

sites is governed by the cation size. Initially, the largest of two cations are known to occupy the A2-sites, while the smaller cations are located at the A1-sites. The C-sites are, if occupied, typically filled by small cations such as Li^+.[5] Furthermore, a certain degree of occupational disorder is expected amid the non-octahedral sites and disorder is increasingly favoured with cation size parity.[6, 7]

The *aristotype* TTB structure has a tetragonal centrosymmetric *P4/mbm* space group, and a whole family of TTB compounds become ferroelectric as they go through one or more phase transitions into non-centrosymmetric space groups.[3] The Curie temperature (T_C) of TTBs is known to depend on composition and is suggested to correlate with factors influencing the chemical bonding such as cation size, coordination, electronic configuration, bond covalency or occupational disorder.[3, 8] The T_C is reported to increase with A-cations radii, with large radii differences between A1 and A2-cations and high degree of ordering within the structure.[6, 8, 9] The displacement of a B-cation away from the octahedral centre in the TTB structure is related to the polarisation and thus also the T_C of a specific TTB composition.[10] The extent of the displacement is determined by several competing factors such as size and charge of the specific B-cations as well as the covalency of the individual B-O bonds.[8, 11-13]

The ferroelectric behaviour of TTBs can range between normal to relaxor ferroelectric. Disorder, on the atomic or charge level, is an important factor to achieve relaxor properties [14]. Materials with properties in the crossover between the two is referred to as diffuse dielectrics.[14-16] TTBs can exhibit relaxations in permittivity data associated with ferroelectric transitions as well as A- and B-site disorder.[16] In normal ferroelectrics disorder relaxations are weak, while stronger disorder relaxations characterise diffuse ferroelectric behaviour. A frequency dispersed peak permittivity is characteristic of relaxor ferroelectrics and can evolve upon the merging of the ferroelectric and disorder relaxations.[16, 17]

The compositional flexibility within the TTB framework, contributes a level of complexity that makes it difficult to predict structure-property relationships. Occupational disorder, which is closely linked to cation size relations, is one factor adding to the complexity but it has to little extent been discussed in relation to its effect on structure and properties. Using a combination of experiment and first principles calculations, we report a systematic study of how the crystal structure and dielectric properties of filled Ba-based TTBs relate to the size of the M-cation in the series of compounds $Ba_4M_2Nb_{10}O_{30}$ (BMN; M=Na, K or Rb) and $Ba_4M_2Nb_8Ti_2O_{30}$ (BMNT; M=Ca or Sr). This is discussed with respect to the level of cation ordering in the A1 and A2 sites. The variation in T_C is correlated to the size of the M-cation cation and the degree of cation disorder on the A sites.

Experimental

Material synthesis
Ba-based tetragonal tungsten bronzes BMN (M = Na, K or Rb) and BMNT (M= Ca or Sr) ceramics were synthesised through a

two-step solid state synthesis route, illustrated in Figure 2. The synthesis of the BMN materials have previously been reported by Nylund and Løndal et al.[7], while the sintering procedure of the three materials is described here. In the first step Nb_2O_5 were separately mixed with Na_2CO_3, K_2CO_3, Rb_2CO_3 and $BaCO_3$ to prepare the niobate precursor compounds $NaNbO_3$, $KNbO_3$, $RbNbO_3$ and $BaNb_2O_6$, respectively. BMNT materials were prepared by mixing $CaCO_3$ or $SrCO_3$ with TiO_2 to prepare $CaTiO_3$ and $SrTiO_3$. The chemicals were dried at 200 °C prior to weighing out stoichiometric amounts followed by mixing in ethanol by

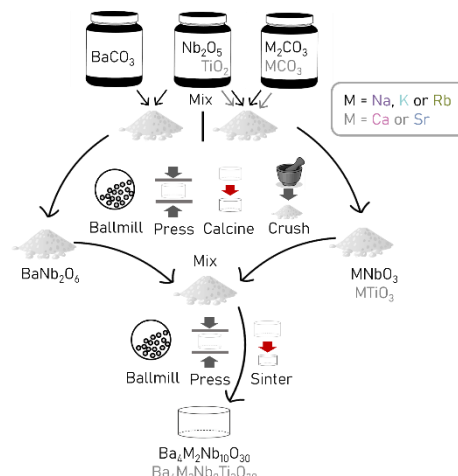Figure 2. Two-step solid state synthesis of $Ba_4M_2Nb_{10}O_{30}$ (M=Na, K, Rb) and $Ba_4M_2Nb_8Ti_2O_{30}$ (M=Ca or Sr) materials.

ball milling for 2 hours. The ethanol was evaporated from the powder mixtures before uniaxially pressing pellets at 30 MPa. The pellets of $NaNbO_3$, $KNbO_3$ and $RbNbO_3$ were prepared by calcination in alumina crucibles with a lid at 700 °C for 4 hours, and then further at 900 °C for 12 hours. $BaNb_2O_6$, $CaTiO_3$, and $SrTiO_3$ was achieved by calcination at 1100 °C for 6 hours.

The precursor pellets were crushed and hand grinded into fine powder in a boron carbide mortar and dried at 120 °C. Powders of $BaNb_2O_6$ were separately mixed with $NaNbO_3$, $KNbO_3$, $RbNbO_3$, $CaTiO_3$ and $SrTiO_3$ in stoichiometric amounts in ethanol by ball milling on a for approximately 24 hours. Ethanol was evaporated from the mixtures before pellets were uniaxially pressed at 40-70 MPa and sintered in alumina crucibles with a lid. To avoid loss of alkali during sintering, the pellets were covered by sacrificial powder of their respective composition. BNN, BCNT and BSNT were sintered at 1285 °C for 6 hours with heating rate of 200 °C/h, BKN was sintered at 1275 °C for 6 hours with heating rate of 300 °C/h and BRN was sintered at 1150 °C for 2 hours with heating rate of 200 °C/h. The sintering procedure was found by trial and error, accompanied by analysis of phase content by qualitative X-ray diffraction. BRN ceramics were sintered by spark plasma sintering (SPS) using a Fuji - Dr Sinter SPS 825. BRN powder was placed in a 12 mm diameter graphite die covered with carbon paper. The instrument was evacuated and an initial pressure of approximately 10 MPa was set. The pressure was gradually increased to 50 MPa while heating the BRN sample from 400 to 900 °C. At constant pressure, the BRN sample was further heated up to and kept at 1015 °C for 2 minutes, before cooled

down to 900 °C. The pressure was then released gradually over 1 minute, before the sample was cooled further to room temperature.

Powders of the sintered ceramics were prepared by crushing and hand grinding in a boron carbide mortar. Prior to crushing, approximately 100 µm of the surface of the sintered pellets was ground of with SiC paper to remove secondary phases, that might have formed due to the known volatility of the alkali oxides.

Material characterisation

The density of the sintered samples was determined by Archimedes method. Theoretical density was calculated from the cell volume and molar mass of each stoichiometric compound. The microstructure of polished surfaces of BNN and BKN and a fracture surface of BRN was imaged by a Hitachi S3400N scanning electron microscopy (SEM). The surfaces of BNN, BKN, BCNT and BSNT were polished with diamond suspension with decreasing particle size down to 0.25 µm and thermally etched at approximately 100 ℃ lower than sintering temperature for 1 minute prior to SEM imaging.

Powder X-ray diffraction patterns of BCNT and BSNT were recorded with a Bruker DaVinci1 diffractometer with Cu Kα radiation, and Rietveld refinement was performed on powder XRD of BNN, BCNT and BSNT acquired at room temperature. The atomic displacement parameters (B_{eq}) from the combined X-ray and neutron diffraction study by Olsen et al. [18] were used and kept constant throughout the refinements. A fundamental parameter model described the peak shape, and the background was described by a Chebychev polynomial of minimal degree. An *Ama*2[19] structure model was used to refine the BCNT and BNN data, and all symmetry inequivalent ion positions were refined. For BSNT a *P4bm* structure[6, 20] was used in the refinement and symmetry inequivalent ion positions for Ba, M, and B-cation positions were refined, while all the O-positions were kept constant. The stoichiometrically constricted occupancies for Ba and M were refined, as described in Table S1 in the supporting information (SI).

Non-ambient temperature powder X-ray diffraction on BKN and BRN was carried out with a Bruker D8 Advance with Cu Kα radiation and a Våntec-1™ SuperSpeed detector. Powder samples were sieved (< 25 um), dispersed in ethanol and dripped onto a Pt-strip. Measurements were recorded every 50 degrees from 30 to 280 °C. The next measurement was recorded at 300 °C, and thereafter measurement was performed every 10 degrees up to 400 °C, before steps of 50 degrees again was used up to 700 °C for both BKN and BRN. Additional measurement with steps of 10 degrees between 220 and 300 °C was performed for BRN in addition. The temperature was calibrated by similar measurement on corundum (Al_2O_3) standard. The lattice parameter evolution upon heating, was acquired through Pawley refinement of each of the non-ambient diffractograms. The refinements were done in sequence from 30 °C, all the way up to 694 °C. Starting parameters from literature [21] were used in the first refinement, and the resulting parameters from each refinement was used in the next.

Rietveld refinements were performed on the BKN and BRN diffractograms obtained at 694 °C. Both BKN and BRN were refined using a *P4/mbm* structure model, adjusted from existing *P4bm* structures[7]. All symmetry inequivalent ion positions were refined. The occupancies were kept constant at values from the reported ambient temperature structure. The atomic displacement parameters (B_{eq}) were kept constant throughout the refinements. A fundamental parameter model described the peak shape, and a background was described by a Chebychev polynomial of minimal degree. For BRN, preferential orientation spherical harmonics polynomial of 4th degree also was included in the refinement.

DSC measurements were carried out on powder samples of all five compounds with a Netzsch DSC 214 Polyma. About 10-20 mg of each sample was placed in an aluminium crucible. An empty aluminium crucible was used as reference. Two consecutive heating cycles from -20 °C to 600 °C were run for each compound. Data from the second heating is presented. A heating/cooling rate of 10 °C per minute, with a hold time of 1 minute at maximum temperature, was used. A mix of synthetic air and nitrogen, with a flow rate of 50 mL/min, was used for gas flow and as protective gas.

Cylindrical disks were prepared for impedance spectroscopy by grinding with SiC-paper, and electrodes were prepared from a platinum paste which were painted on the surface and baked at 900 °C for 10 minutes. Impedance spectroscopy up to 400 °C was carried out with an Novocontrol Alpha-A HVB 4000 impedance analyzer with BDS 1200 HV sample cell and a NOVOTHERM temperature controller, while for measurements above 400 °C a Norecs ProboStat A-5 sample cell in a tubular furnace connected to a Eurotherm 2408 temperature controller was used. Data was collected through the Novocontrol WinDETA software at 45 frequencies between 10^{-2} and 10^7 Hz at each set temperature. Heating/cooling rates were set to 2℃ per minute. For each composition there was a slightly different configuration for the temperature dependent measurements (Table S4 in SI). For all five compounds data from heating during the 2nd cycle is reported. For BNN measurements were carried out in the range 30-400 °C (Alpha A) and 400-600 °C (Probostat) in individual sets of measurement. For BSNT two sets of measurements, with two heating-cooling cycles in each, was carried out on the same sample with a few days between.

Ferroelectric hysteresis measurements were carried out on BNN, BKN and BRN ceramics with painted-on Pt electrodes, using aixACCT aixPES Piezoelectric Evaluation System. The samples were measured in steps of 10 kV/cm from at 100 Hz. At selected field strengths measurements were also done at a range of frequencies. For BNN and BKN, measurements were also carried out at temperatures up to 220 and 150 °C, respectively.

Computational Methods

Density functional theory (DFT) calculations were achieved using the Vienna ab initio Simulation Package (VASP)[22-25]. The projector-augmented wave method (PAW)[26] was used to describe the interactions between the core and valence

electrons (Na[He], K[Ne], Rb[Ar], Ca[Ar], Sr[Kr], Ba[Xe], Nb[Kr], O[He]) for each R_2MNb$_5$O$_{15}$ (M=Na, K, Rb; R = Ca, Sr, Ba) composition studied herein. The PBEsol (Perdew-Burke-Ernzerhof) functional[27, 28] was used in this study and consistently gave good descriptions of the structural properties of a material relative to experiment. In particular, PBEsol has been used to successfully determine ionic disorder and alloying[29, 30]. Initially a full geometry relaxation of the lattice parameters and ionic positions of fully ordered and stoichiometric R_2MNb$_5$O$_{15}$ (in the $P4/mbm$ aristotype spacegroup) were performed. A plane wave energy cut-off of 500 eV and a Γ-centred k-point grid of 2×2×6 was used, and convergence was regarded as complete when the maximum force on any atom was below 0.01 eV Å-1. Tabulated structural properties are provided in SI Table S6-S9. Phonon dispersions were calculated using finite-displacements as implemented in Phonopy[31] and plotted using the open-source sumo[32] package. A 1×1×3 supercell was sufficient to describe the imaginary frequencies in R_2MNb$_5$O$_{15}$. Understanding the unstable frequencies took the form of phonon modemapping using "ModeMap"[33] which has been shown to successfully determine displacive transitions in other materials[33, 34].

Thermodynamics of Cation Site Disorder

The Site Occupancy Disorder (SOD) program[35] by Grau-Crespo et al. was used alongside the python package bsym[36] to determine symmetry inequivalent configurations within the ensemble method. 1x1x2 supercells of each R_2MNb$_5$O$_{15}$ ($P4/mbm$) composition were generated and fully relaxed using a k-point grid of 2x2x3 to the same convergence criteria as the fully ordered R_2MNb$_5$O$_{15}$ compositions.

Within the SOD algorithm, Boltzmann probabilities (P_m) are used to determine the existence of a particular unique configuration[37], m:

$$\widetilde{P}_m \;=\; \frac{1}{Z}\Omega_m \exp\frac{-E_m}{k_BT} = \frac{1}{Z}\exp\frac{-\widetilde{E}_m}{k_BT}$$

Which depends on the energy of a given configuration (E_m)

and its degeneracy (Ω_m) and is related to temperature (T) through the Boltzmann's constant (k_B). Z is the partition function, and is described by:

$$Z = \sum_{m=1}^{M} \exp(-\widetilde{E}_m/k_BT)$$

Where the reduced energy, $-\widetilde{E}_m$, is given by:

$$\widetilde{E}_m = E_m - T\widetilde{S}_m$$

And the degeneracy entropy, $\widetilde{S}_m$:

$$\widetilde{S}_m = k_BT \ln \Omega_m$$

The configurational free energy, G, can be obtained thus:

$$G = -k_BT\, ln(Z)$$

P_m can be used to gain a weighted average of an observable quantity (Q) such as the lattice parameters, electronic properties, NbO$_6$ octahedral tilting etc.:

$$Q = \sum_{m=1}^{M} P_m Q_m$$

Where M is the total number of inequivalent configurations for a particular configuration.

Further calculations to understand the influence of cation site disorder and the bonding nature of the NbO$_6$ octahedral framework were carried out using a crystal orbital Hamiltonian population (COHP) analysis within the Lobster package[38] aided by lobsterpy[39-41].

The tabulated list of configurations and their degeneracy are given in Table S9 in SI.

Results

Crystal structure and microstructure

Phase pure ceramics of BNN, BKN, BCNT and BSNT were

Table 1. Summary of the lattice parameters, the occupancy on the A1 and A2 sites, density and the Curie temperature of the materials studied in this work.

Compound	Space group	a and b [Å]	c [Å]	Occupancy of M on A1 site	Occupancy of Ba on A2 site	Theoretical density [g/cm³]	Relative density [%]	TC [∘C]
BNN (*M*=Na)	Ama2	17.63258(18) 35.2036(4)	7.98157(7)	0.885(5)	0.942(2)	5.3744	92	550
	$P4/mbm^{41}$	12.56245	3.98107	-	-			
BKN (*M*=K)	$P4bm^7$	12.55436(15)	4.02163(6)	0.475(6)	0.7525(19)	5.3353	91	320
	$P4/mbm$	12.64380(14)	3.99955(6)	0.475	0.273			
BRN (*M*=Rb)	$P4bm^7$	12.59930(9)	4.02539(3)	0.141(7)	0.570(4)	5.5334	97	270
	$P4/mbm$	12.69931(19)	4.00135(5)	0.141	0.570			
BCNT (*M*=Ca)	Ama2	17.5496(5) 35.0496(10)	7.90578(16)	0.932(9)	0.966(4)	5.3228	89	210
BSNT (*M*=Sr)	$P4bm$	12.4769(2)	3.96636(8)	0.737(12)	0.869(6)	5.4958	91	100‡

‡Temperature of peak permittivity at 1 kHz

obtained through the two-step solid-state synthesis procedure (Figure 1), while minor traces of a secondary phase ($Rb_4Nb_6O_{17} \cdot 3H_2O$) were identified in BRN. Relative densities in
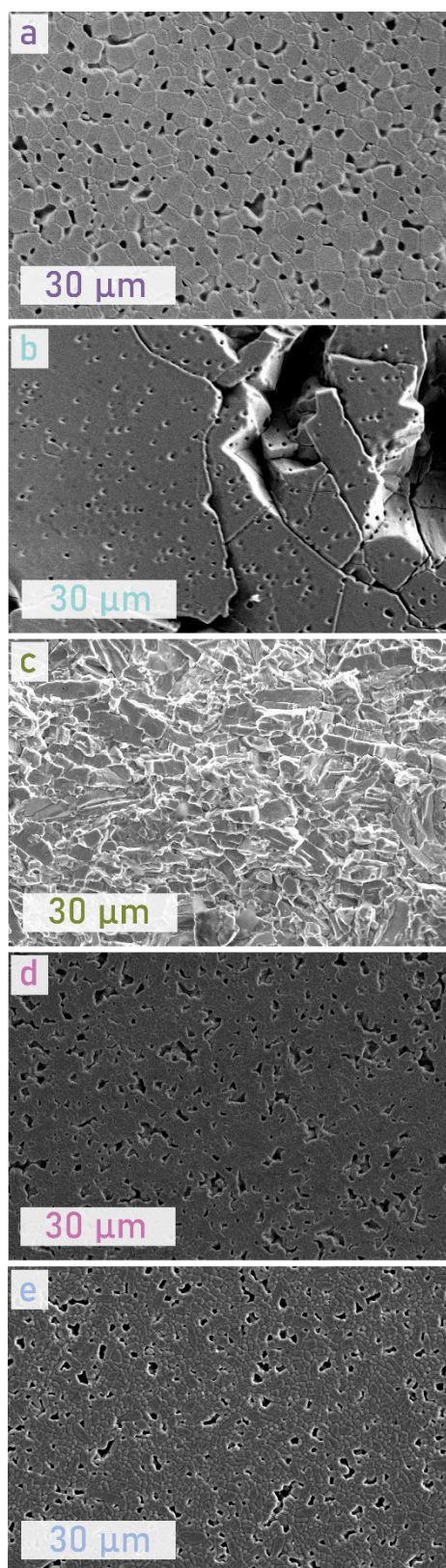

Figure 3. SEM images of polished surfaces of BNN (a) and BKN (b), of fracture surface of BRN (c), polished surface of (d) BCNT and (e) BSNT.

the range 89-92 % (Table 1) were achieved for BNN, BKN, BCNT and BSNT ceramics through conventional solid-state sintering, while for BRN a relative density of 97 % was achieved through spark plasma sintering. Conventional sintering of BRN did not result in ceramics with sufficient density for electrical characterization. The microstructure of polished surfaces of BNN, BKN, BCNT and BSNT, as well as a fracture surface of BRN are displayed in Figure 3. The grain size is below 5 μm for BCNT and BSNT, below 10 μm for BNN and range from close to 10 μm to larger than 100 μm for BKN. Closed circular pores inside grains are evident in BKN, indicative of rapid grain growth during densification. The microstructure of BRN is influenced by the lower temperature applied during SPS, and the plate-like grains align horizontally in the plane which is normal to the pressing direction. Rietveld refinements of BCNT and BSNT, respectively, using the *Ama*2 and *P4bm* TTB crystal structure respectively, are shown in Figure 4. The crystallographic data determined by the Rietveld refinements, including occupation of cations on both A- and B-sites, are summarized in Table 2 and Table 3. The Rietveld refinement of BNN using the *Ama*2 space group is shown in Figure S1 and summarized in Table S2 in SI. Rietveld refinement of BCNT using the *Cmm*2 space group is included in Table S3.

Rietveld refinement of X-ray diffractograms of BKN and BRN, acquired at ambient temperature were reported in a previous paper[7]. The crystallographic data, for all five compositions, including the space group, lattice parameters and occupation of M-cation on A1 site are included in Table 1. The ambient temperature lattice parameters increase systematically with the size of M. BCNT was refined towards the same orthorhombic crystal structure as reported for BNN[19, 43], while BSNT have the same tetragonal crystal structure as reported for BKN and BRN. Thus, the two compounds with the smallest M-cations have orthorhombic symmetry, while the compounds with larger M-cations have a tetragonal symmetry. The occupation of M- cations on the A1-site in BCNT and BSNT decrease systematically with increasing size of the M-cation, in line with previous report on BNN, BKN and BRN.[7] With introduction of titanium in BCNT and BSNT, occupational
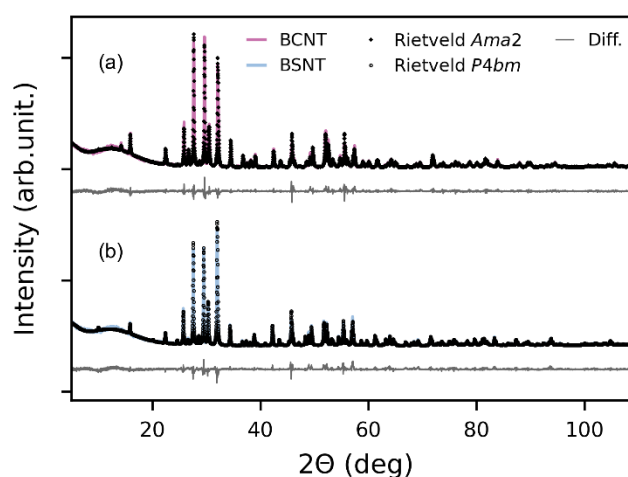

Figure 4. Xray diffractograms for (a) BCNT and (b) BSNT with respective Rietveld refinement towards *Ama*2 and *P4bm* space groups

disorder is also possible on the two B-sites. The occupation of Ti on the B1 sites is slightly higher than the nominal composition (0.2 Ti) with occupation of 0.29 and 0.23, respectively, compared to for BCNT and BSNT.

Table 2. Refined *Ama*2 crystal structure of $Ba_4Ca_2Nb_8Ti_2O_{30}$. The number of independent parameters that were refined was 168. Unit cell parameters: a = 17.5496(5) Å, b = 35.0493(10) Å and c = 7.90574(15) Å. GOF: 1.99, Rwp: 11.23. Refined parameters are in **bold**.

Site	Mp	Atom	X	Y	Z	Occupancy	Beq
A2_1	8	Ba	**0.9216(17)**	**0.8758(10)**	**0.229(5)**	**0.966(4)**	0.44
		Ca				**0.034(4)**	0.44
A2_2	8	Ba	**0.0780(16)**	**0.6224(7)**	**0.236(6)**	**0.966(4)**	0.44
		Ca				**0.034(4)**	0.44
A2_3	4	Ba	0.25000	**0.9605(17)**	**0.240(8)**	**0.966(4)**	0.44
		Ca				**0.034(4)**	0.44
A2_4	4	Ba	0.75000	**0.5397(16)**	**0.239(8)**	**0.966(4)**	0.44
		Ca				**0.034(4)**	0.44
A2_5	4	Ba	0.25000	**0.7887(14)**	**0.245(8)**	**0.966(4)**	0.44
		Ca				**0.034(4)**	0.44
A2_6	4	Ba	0.75000	**0.7104(15)**	**0.257(7)**	**0.966(4)**	0.44
		Ca				**0.034(4)**	0.44
A1_1	8	Ca	**0.499(6)**	**0.749(4)**	**0.257(12)**	**0.963(8)**	1.6
		Ba				**0.068(9)**	1.6
A1_2	4	Ca	0.00000	0.00000	**0.26(2)**	**0.963(8)**	1.6
		Ba				**0.068(9)**	1.6
A1_3	4	Ca	0.00000	0.50000	**0.287(13)**	**0.963(8)**	1.6
		Ba				**0.068(9)**	1.6
B1_1	4	Nb	0.75000	**0.124(3)**	0.00000	**0.705(19)**	0.42
		Ti				**0.295(19)**	0.42
B1_2	4	Nb	0.25000	**0.374(3)**	0.00000	**0.705(19)**	0.42
		Ti				**0.295(19)**	0.42
B1_3	4	Nb	0.75000	**0.875(4)**	0.00000	**0.705(19)**	0.42
		Ti				**0.295(19)**	0.42
B1_4	4	Nb	0.25000	**0.624(4)**	0.00000	**0.705(19)**	0.42
		Ti				**0.295(19)**	0.42
B2_1	8	Nb	**0.642(5)**	**0.784(2)**	**-0.019(6)**	**0.824(5)**	0.42
		Ti				**0.176(5)**	0.42
B2_2	8	Nb	**0.357(5)**	**0.715(3)**	**0.005(7)**	**0.824(5)**	0.42
		Ti				**0.176(5)**	0.42
B2_3	8	Nb	**0.858(5)**	**0.966(2)**	**-0.005(6)**	**0.824(5)**	0.42
		Ti				**0.176(5)**	0.42
B2_4	8	Nb	**0.142(5)**	**0.535(2)**	**0.004(6)**	**0.824(5)**	0.42
		Ti				**0.176(5)**	0.42
B2_5	8	Nb	**0.430(5)**	**0.821(2)**	**-0.008(6)**	**0.824(5)**	0.42
		Ti				**0.176(5)**	0.42
B2_6	8	Nb	**0.570(5)**	**0.679(2)**	**-0.004(6)**	**0.824(5)**	0.42
		Ti				**0.176(5)**	0.42
B2_7	8	Nb	**0.068(5)**	**0.928(2)**	**0.013(7)**	**0.824(5)**	0.42
		Ti				**0.176(5)**	0.42
B2_8	8	Nb	**0.929(5)**	**0.571(2)**	**0.002(7)**	**0.824(5)**	0.42
		Ti				**0.176(5)**	0.42
O1_1	8	O	**0.03(2)**	**0.874(13)**	**-0.04(4)**	1	1.17
O1_2	8	O	**0.97(2)**	**0.624(13)**	**-0.04(4)**	1	1.17
O1_3	4	O	0.25000	**0.014(16)**	**0.04(5)**	1	1.17
O1_4	4	O	0.75000	**0.487(17)**	**0.02(5)**	1	1.17
O1_5	4	O	0.25000	**0.238(19)**	**-0.03(4)**	1	1.17
O1_6	4	O	0.75000	**0.263(19)**	**-0.00(5)**	1	1.17
O2_1	8	O	**0.61(2)**	**0.232(11)**	**-0.02(4)**	1	1.17
O2_2	8	O	**0.40(2)**	**0.271(10)**	**-0.09(3)**	1	1.17
O2_3	8	O	**0.892(11)**	**0.026(6)**	**-0.16(2)**	1	1.17
O2_4	8	O	**0.11(2)**	**0.481(11)**	**-0.01(4)**	1	1.17
O2_5	8	O	**0.54(2)**	**0.803(12)**	**-0.06(4)**	1	1.17

Site	Mp	Atom	X	Y	Z	Occupancy	Beq
O2_6	8	O	**0.462(19)**	**0.695(10)**	**-0.00(4)**	1	1.17
O2_7	8	O	**0.969(12)**	**0.957(5)**	**0.00(4)**	1	1.17
O2_8	8	O	**0.04(2)**	**0.551(9)**	**-0.08(4)**	1	1.17
O3_1	8	O	**0.68(3)**	**0.166(14)**	**-0.02(4)**	1	1.17
O3_2	8	O	**0.32(2)**	**0.333(13)**	**-0.05(4)**	1	1.17
O3_3	8	O	**0.82(2)**	**0.084(12)**	**-0.05(4)**	1	1.17
O3_4	8	O	**0.18(2)**	**0.415(13)**	**-0.01(3)**	1	1.17
O3_5	8	O	**0.67(2)**	**0.837(12)**	**-0.05(3)**	1	1.17
O3_6	8	O	**0.33(3)**	**0.662(13)**	**0.01(4)**	1	1.17
O3_7	8	O	**0.83(2)**	**0.913(12)**	**0.03(4)**	1	1.17
O3_8	8	O	**0.17(2)**	**0.588(13)**	**-0.00(3)**	1	1.17
O4_1	8	O	**0.875(16)**	**0.792(8)**	**0.24(5)**	1	1.17
O4_2	8	O	**0.144(18)**	**0.731(7)**	**0.24(4)**	1	1.17
O4_3	8	O	**0.649(19)**	**0.980(8)**	**0.25(5)**	1	1.17
O4_4	8	O	**0.368(17)**	**0.540(8)**	**0.24(4)**	1	1.17
O4_5	8	O	**0.414(14)**	**0.941(6)**	**0.24(4)**	1	1.17
O4_6	8	O	**0.554(16)**	**0.573(9)**	**0.25(4)**	1	1.17
O4_7	8	O	**0.082(15)**	**0.816(7)**	**0.24(4)**	1	1.17
O4_8	8	O	**0.953(17)**	**0.676(9)**	**0.25(4)**	1	1.17
O5_1	4	O	0.75000	**0.865(12)**	**0.25(6)**	1	1.17
O5_2	4	O	0.25000	**0.614(12)**	**0.27(5)**	1	1.17
O6_1	4	O	0.75000	**0.112(11)**	**0.26(6)**	1	1.17
O6_2	4	O	0.25000	**0.364(11)**	**0.27(5)**	1	1.17

Table 3. . Refined *P4bm* crystal structure of $Ba_4Sr_2Nb_8Ti_2O_{30}$ at 293 ℃. The number of independent parameters that were refined was 33. Unit cell parameters: a = 12.4769(2) Å and c = 3.96636(8) Å. GOF: 2.11, Rwp: 12.64. Refined parameters are in **bold**.

Site	Mp	Atom	X	Y	Z	Occupancy	Beq
A2	4	Ba	**0.17188(13)**	**0.67188(13)**	**0.416(6)**	**0.869(6)**	0.44
		Sr				**0.131(6)**	0.44
A1	2	Sr	0.00000	0.00000	**0.429(7)**	**0.737(12)**	1.6
		Ba				**0.263(12)**	1.6
B1	2	Nb	0.00000	0.50000	**-0.043(6)**	**0.764(13)**	0.42
	2	Ti				**0.236(13)**	0.42
B2	8	Nb	**0.07438(18)**	**0.21434(17)**	**-0.065(5)**	**0.809(3)**	0.42
	8	Ti				**0.191(3)**	0.42
O1	8	O	0.34068	0.00685	-0.094	1	1.17
O2	8	O	0.14096	0.07107	-0.1003	1	1.17
O3	4	O	0.28565	0.78565	-0.0934	1	1.17
O4	2	O	0.00000	0.50000	0.4148	1	1.17
O5	8	O	0.29336	0.42747	0.4194	1	1.17

Thermal evolution of crystal structure of BKN and BRN

In Figure 5, representative XRD patterns of BKN and BRN acquired upon heating are presented. The ferroelectric phase transition taking place is not easily observed as no extinction of diffraction lines take place in the transition from *P4bm* to *P4/mbm*. However, a splitting of overlapping diffraction lines occurs as the contraction in c-direction moves respective diffraction lines opposite to the shift caused by of thermal expansion upon heating. At approximately 22° and 30° 2Ɵ, the splitting of the (001)/(310) and the (221)/(330) diffraction lines is visible. The splitting is more visible in BKN than in BRN, where the splitting is only visible as a shoulder evolving in the (221)/330 reflections. The clearer splitting in BKN is caused by the larger temperature interval in which the shifts are allowed to evolve in BKN compared to BRN. The thermal evolution of the lattice parameters of BKN and BRN, found from the Pawley refinement of the XRD patterns (Figure 5) is shown in Figure 6, together with the corresponding data for BNN from literature.[42] Thermal expansion of the in-plane parameter (Figure 5 (a)) is evident for both BKN and BRN, while a contraction of the out-of-plane parameter (Figure 5 (b)) is observed upon heating, demonstrating that a phase transition takes place at ~320 °C for BKN and ~270 °C for BRN. This behaviour is qualitatively similar to the ferroelectric phase transition reported for BNN at 570 °C.

Rietveld refinement of the diffraction patterns of BKN and BRN at 694 °C are shown in Figure 7 using the *P4/mbm aristotype* TTB crystal structure. The crystallographic data determined by the Rietveld refinements are summarized in Table 4 and Table 5, and the lattice parameters are included in Table 1.
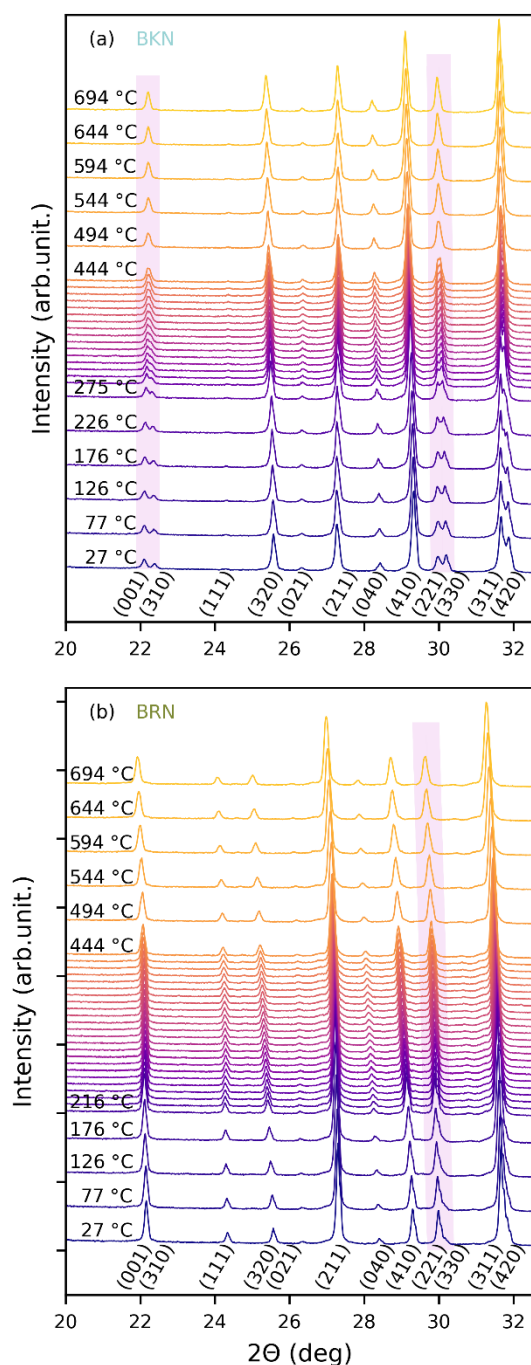
Figure 5. XRD patterns of (a) $Ba_4K_2Nb_{10}O_{30}$ and (b) $Ba_4Rb_2Nb_{10}O_{30}$ acquired at various temperatures upon heating. The (hkl) indexing is done according to the P4/mbm TTB aristotype. The diffractograms which are not labelled with temperature were measured with 10 degrees steps. Shaded lines at ~ 22° and ~30° 2θ, highlight the (001)/(310) and the (221)/(330) diffraction lines, respectively.
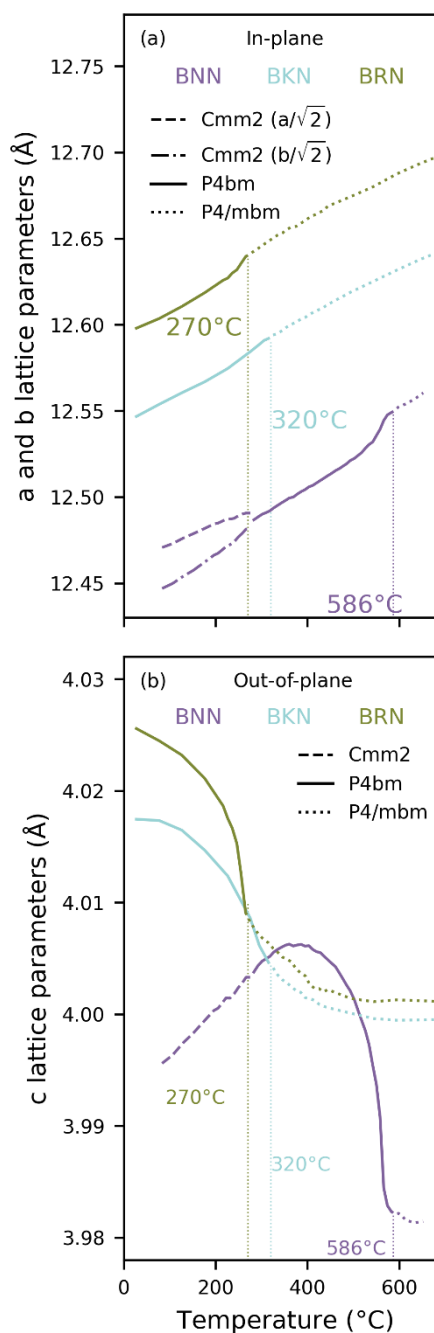

Figure 6. In plane (a) and out of plane (b) lattice parameter evolution as a function of temperature from Pawley refinement on non-ambient temperature XRD data for $Ba_4Na_2Nb_{10}O_{30}$ (from ref- 41), $Ba_4K_2Nb_{10}O_{30}$ and $Ba_4Rb_2Nb_{10}O_{30}$.

Table 4. Refined *P4/mbm* crystal structure of $Ba_4K_2Nb_{10}O_{30}$ at 694 °C. The number of independent parameters that were refined was 30 Unit cell-parameters: a = 12.64380(14) Å and c = 3.99955(6) Å. GOF: 2.47, Rwp: 6.77. Refined parameters are in **bold**.

Site	Mp	Atom	X	Y	Z	Occupancy	Beq
A2	4	Ba	**0.1744(2)**	**0.6744(2)**	0.5000	0.753	0.44
		K				0.246	0.44
A1	2	K	0.00000	0.00000	0.50000	0.505	1.6
		Ba				0.495	1.6
Nb1	2	Nb	0.00000	0.50000	0.00000	1	0.42
Nb2	8	Nb	**0.0724(2)**	**0.2125(2)**	0.00000	1	0.42
O1	8	O	**0.3483(18)**	**0.0168(11)**	0.00000	1	1.17
O2	8	O	**0.1390(13)**	**0.0733(16)**	0.00000	1	1.17
O3	4	O	**0.2650(12)**	**0.7650(12)**	0.00000	1	1.17
O4	2	O	0.00000	0.50000	0.50000	1	1.17
O5	8	O	**0.2853(12)**	**0.4256(16)**	0.50000	1	1.17

Table 5. Refined *P4/mbm* crystal structure of $Ba_4Rb_2Nb_{10}O_{30}$ at 694 °C. The number of independent parameters that were refined was 33. Unit cell parameters: a = 12.69931(19) Å and c = 4.00135(5) Å. GOF: 2.13, Rwp: 5.92. Refined parameters are in **bold**.

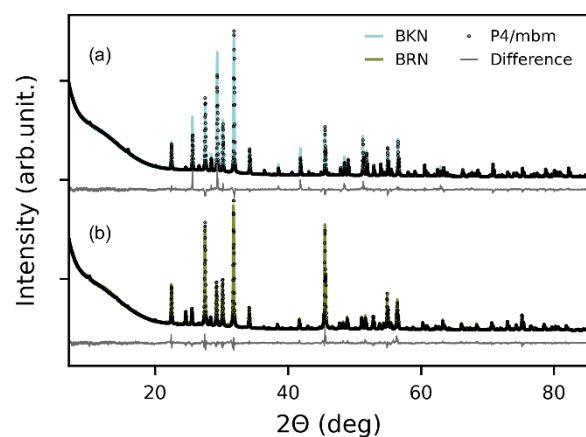| Site	Mp	Atom	X	Y	Z	Occupancy	Beq
A2	4	Ba	**0.1740(2)**	**0.6740(2)**	0.5000	0.570	0.44
		Rb				0.430	0.44
A1	2	Rb	0.00000	0.00000	0.5000	0.141	1.6
		Ba				0.859	1.6
Nb1	2	Nb	0.00000	0.50000	0.00000	1	0.42
Nb2	8	Nb	**0.0743(3)**	**0.2151(2)**	0.00000	1	0.42
O1	8	O	**0.3390(17)**	**0.0244(13)**	0.00000	1	1.17
O2	8	O	**0.1395(14)**	**0.0720(19)**	0.00000	1	1.17
O3	4	O	**0.2820(15)**	**0.7820(15)**	0.00000	1	1.17
O4	2	O	0.00000	0.50000	0.50000	1	1.17
O5	8	O	**0.2811(14)**	**0.4249(17)**	0.50000	1	1.17

Figure 7. X-ray diffractograms (a) $Ba_4K_2Nb_{10}O_{30}$ and (b) $Ba_4Rb_2Nb_{10}O_{30}$ at 694 °C together with Rietveld refinement to the *P4/mbm* space group.

Dielectric properties

The frequency dependence of the dielectric permittivity as function of temperature for the BMN-series (a-c) and for the BMNT-series (d-e) are presented in Figure 8. Additional results from impedance spectroscopy are presented in Figure S2-S7 in SI. A maximum in the permittivity corresponding to the ferroelectric-to-paraelectric phase transition is evident for BNN, BKN and BRN at temperatures of 550, 320 and 270 °C, respectively. The phase transition temperature is shifted to lower temperature with increasing size of the M-cation within the BMN series.

BCNT exhibits a maximum in the permittivity at 210 °C. A second relaxation, associated with frequency dispersion, is seen at higher temperatures (Figure S5 in SI). BSNT evinces a pronounced frequency dispersion in the dielectric permittivity, demonstrated by the shift of the maximum permittivity to higher temperatures for higher frequencies. However, at first no frequency dispersion is observed. The frequency dispersion develops with thermal cycling (Figure S7 in SI) and eventually stretches over several hundred degrees.

In the first of two sets of measurements (Figure S7 (a-d)) the frequency dispersion did not appear until the second cooling. Upon the first heating and cooling the peak permittivity is stable at just under 100 °C for all frequencies. In the first heating, a second peak is observed at about 300 °C in the low frequency regime. The same peak is not observed during the first cooling. In the second heating, frequency dispersion is observed at the maximum permittivity, as well as a second peak again is visible at about 300 °C, but now in the high frequency regime. In the
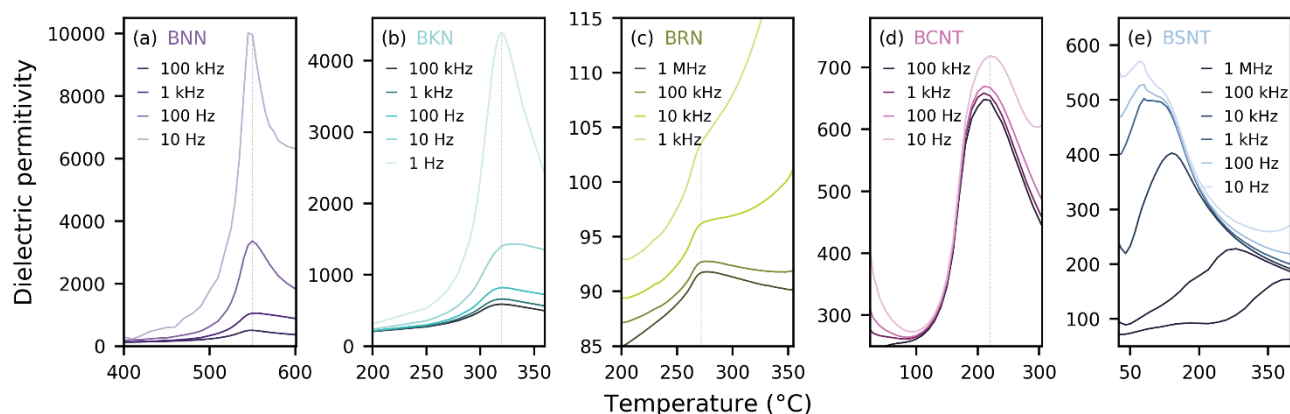
Figure 8. Dielectric permittivity as function of temperature. Peak permittivity is observed for (a) $Ba_4Na_2Nb_{10}O_{30}$ at 550 °C, (b) $Ba_4K_2Nb_{10}O_{30}$ at 320 °C, (c) $Ba_4Rb_2Nb_{10}O_{30}$ at 270 °C d) $Ba_4Ca_2Nb_8Ti_2O_{30}$ at 210 °C, and a pronounced frequency dispersion with maximum at higher temperature for higher frequencies for (e) $Ba_4Sr_2Nb_8Ti_2O_{30}$. The data presented for all compounds, except BSNT, is from the second heating. For BSNT the data presented is from the second heating of a second round of measurements.

second cooling the frequency dispersion apparently stretched over several hundred degrees. In the second set of measurements (Figure S7 (e-h)) on the same sample, again no frequency dispersion is observed in the first heating, but like in the first set of measurements, a second peak is visible around 300 °C, but now in a wider frequency range. On the first cooling the same level of frequency dispersion, as seen in the second cooling of the first set of measurements, is observed. The diffusive dielectric relaxations observed for BSNT appear to rise from more than one phenomenon that develop overlapping frequency dispersions upon thermal cycling.

The DSC data (Figure S8-S10 in SI) show that BNN, BKN, BRN and BCNT have endothermic peaks corresponding with the ferroelectric phase transitions. The diffusive ferroelectric phase transition observed for BSNT is supported by the lack of a peak in the DSC data.

Polarisation-field and strain-field hysteresis measurements
Polarisation-electric field (PE) loops measured at 100 Hz at room temperature for BMN and BMNT compounds are shown in Figure 9. Strain-electric field response (S-E) loops as well as PE-loops measured at a range of frequencies and temperatures are presented in Figure S11-14 in SI. BNN, BKN, BCNT and BSNT show Polarisation-Electric Field (PE) loops for ceramic TTBs, with relatively low maximum and remnant polarisation. BRN shows typical behaviour of a lossy dielectric. The bipolar strain is to a large degree symmetric for all five compounds, but to a lesser degree compared to their respective P-E loops.

At maximum field of 100 kV/cm for BNN, the maximum polarisation reached 5.0 µC/cm², while the remnant polarisation (Pr) was 2.2 µC/cm² (Figure 9(a)). The strain of BNN (Figure S11 (a)) is positive with a maximum displacement of 0.007 %. A slight frequency dependence is observed in the range 20-100 Hz at ambient temperature (Figure S13 (a)). Upon heating, the PE-loops of BNN become slimmer with increasing temperature up to 200 °C (Figure S15 (a)), which also leads to a decrease of remnant polarisation. At elevated temperature the PE-loops are more stable with respect to frequency (Figure S15 (b)).

For BKN at 90 kV/cm the maximum polarisation was 6.1 µC/cm², Pr was 2.0 µC/cm² (Figure 9(b)) and a negative strain of -0.008 to -0.01 % (Figure S11 (b)). Upon heating up to 150 °C the P-E-loops show some asymmetry as the negative electric field half of the field cycle narrow slightly (Figure S16 (a)). Asymmetry also manifests in the strain behaviour at elevated temperatures, where a positive strain is observed in the negative field region, as well as a general broadening of the loop (Figure S16 (a)).

BRN shows behaviour of a dielectric with high loss. The PE-loops are rounded with a maximum polarisation of about 2 µC/cm² (Figure 9(c)) and the SE-loops show a negative strain of -0.004% at 70 kV/cm (Figure S11 (c)). The PE-loop show large frequency dependence in the range 100-20 Hz (Figure S13 (c)).

BCNT possesses a maximum polarisation of 2.7 µC/cm², a Pr of 0.75 µC/cm² (Figure 9 (d)) and positive strain of 0.003 % (Figure S12 (a)) at 70 kV/cm. The compound demonstrates high stability of PE-loops with respect to frequency in the range 100-20 Hz (Figure S14 (a)), as well as temperatures up to 175 °C (Figure S17 (a)). At field of 100 kV/cm the maximum polarisation was 4.5 µC/cm² and Pr was 1.2 µC/cm² for BCNT at 175 °C (Figure S17 (c)).

At 60 kV/cm BSNT reached a maximum polarisation of 6.2 µC/cm² and Pr of 2.0 µC/cm² (Figure 9 (e)). The PE-loops show high stability with respect to frequency in the range 100-10 Hz (Figure S14 (b)). Some asymmetry is observed in the SE-loops and positive strain maximum range from 0.004 to 0.008 % (Figure S12(b)). The compound has not been measured at elevated temperatures.
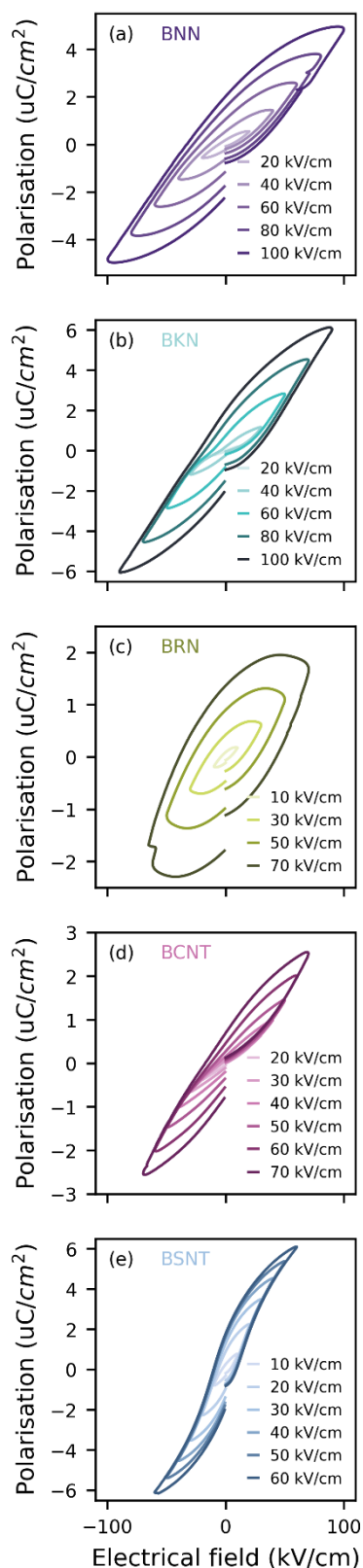
Figure 9. Polarisation-Electric field loops measured on (a) BNN (20-100 kV/cm), (b) BKN (40-100 kV/cm), (c) BRN (10-70 kV/cm) at 100 Hz, (d) BCNT (20-70 kV/cm) and (e) BSNT (10-60 kV/cm)) at 100 Hz and ambient temperature.

Ab initio Thermodynamics

Figure 10 shows the anharmonic double wells for R = Ca (a), Sr (b), Ba (c)-based TTB compositions at the lowest imaginary frequency Γ mode as shown in the phonon dispersion plots in Figure S19 in SI. All compositions, with the exception of $Ca_2RbNb_5O_{15}$, demonstrate symmetrical anharmonic double wells where the minima give rise to the *P4bm* ferroelectric structure. $Ca_2RbNb_5O_{15}$ shows a slight energy lowering off the starting configuration, which is shown in SI Figure 20, and as such is not included in the double well analysis. The phase transition mechanism at Γ shows a modulation of the Nb-O sublattice within the c-direction in keeping with previous work.[6, 42]

Figure 10 (d) shows the well depth (ΔE) as a function of overall TTB tolerance factor.[4] In general, there is a trend towards a larger ΔE as the tolerance factor increases, heavily influenced by the "nominal" A2 site cation radii (Ca, Sr, and Ba, with r=1.34, 1.44, 1.61 Å, respectively [44]). At larger ΔE, a higher T_C is expected due to the increased energy required to overcome the structural transformation. This trend is seen experimentally between Ca, Sr and Ba compositions (i.e., $Ca_2KNb_5O_{15}$ (378 K [45]), $Sr_2KNb_5O_{15}$ (429 K [21, 46]), $Ba_2KNb_5O_{15}$ (665 K [21, 46])), however the trend between nominal A1-cations (Na, K, and Rb) does not follow the trend seen in experiment where there is a decrease in T_C with increasing r_{A1}. Thus, it can be speculated that in an idealised situation where the compositions are both stoichiometric and ordered, one would expect the T_C to drop in the order Rb-K-Na. It has been seen previously that 2-4 perovskites such as $BaTiO_3$ also show a decreasing T_C with increasing tolerance factor [47]. The amplitude difference (ΔQ) in general follows the A2 trend, in particular, when considering the A2 site tolerance factor (TF_{A2}) which can be seen in Figure S21 in SI. On average, ΔQ increases in the order Ca-Sr-Ba, which, when combined with a shallower ΔE, suggests a tendency towards *dynamic disorder* between the two structures[48], thus a likely ambiguity towards where the T_C lies.
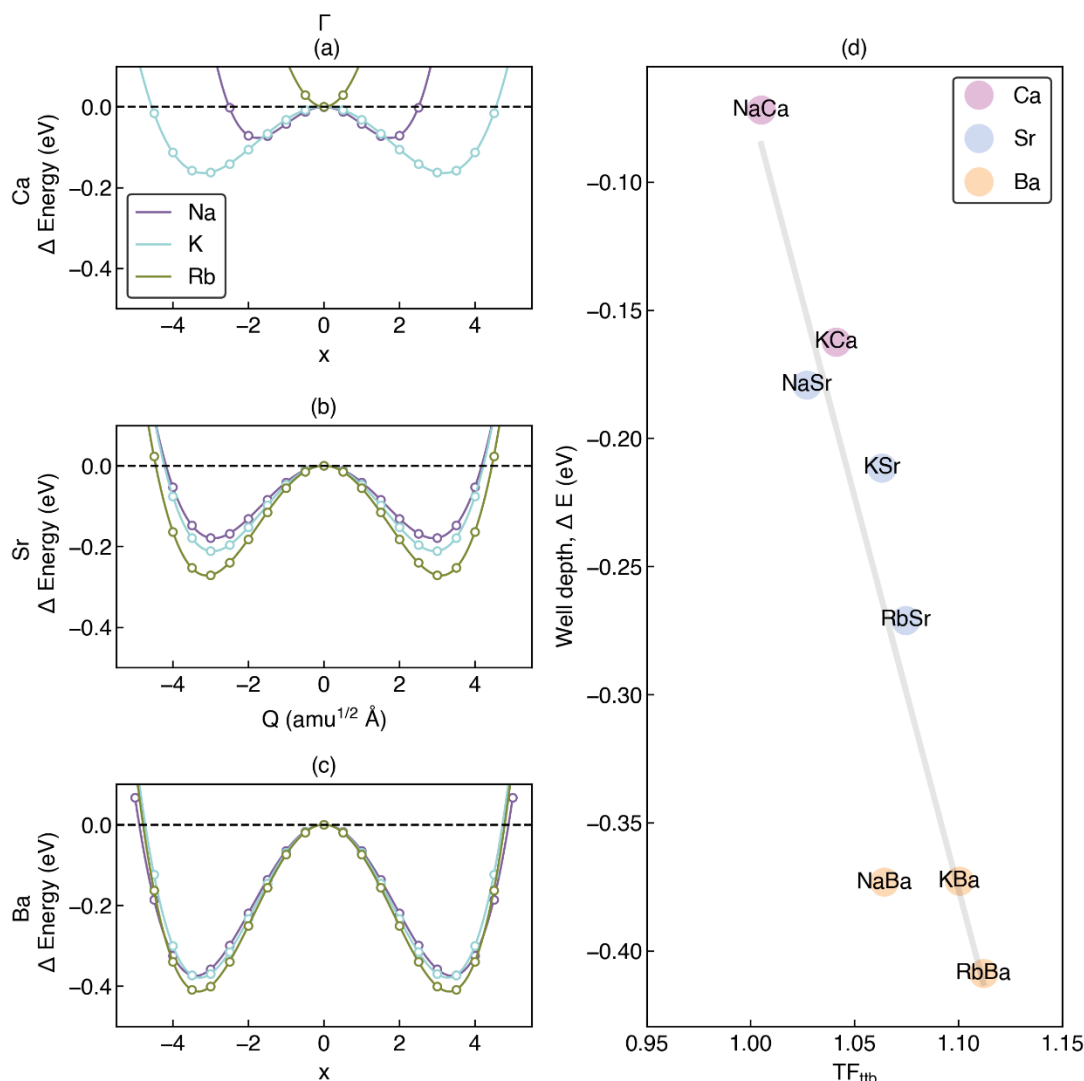
Figure 10. The anharmonic double wells for R = Ca (a), Sr (b), Ba (c)-based TTB compositions along the Γ_1 mode. In (d), the anharmonic well depths ΔE are shown as a function of TTB tolerance factor (TF_{ttb}). A tighter Q range is given for $Ca_2RbNb_5O_{15}$ in SI Figure X which shows the absence of a double well but an infinitesimally small energy lowering off the starting configuration. As such it is not included in the analysis here.

Thermodynamics of Cation Site Disorder

Figure 11 shows the calculated Gibbs free energies ΔG (a-c) and tetragonality, c/a, (d-f) for R=Ca, Sr, Ba, respectively, (left to right columns) as a function of A-site disorder within the $P4/mbm$ aristotype space group. Additional data regarding Nb-O-Nb angles in the c-direction and antibonding Nb-O character of the valence band are given in Figure S22 in SI.

The A-site cation disorder is calculated in such a way that 0 % "M on A1 site" corresponds to M = Na, K, Rb existing solely on the A2-cation site, whilst at 100 % the M-cation exists purely on its intended A1-site within the TTB structure. In total, 9 compositions were calculated in order to understand the influence of A-cation size on the thermodynamics and properties of the TTB structure.

In the Ba-based TTB compositions in Figure 11 (c) it is seen that with increasing ionic radii of the M-cation, there is a heightened preference towards A2-site occupation. These results are consistent with the experimental XRD data in previous work[7] and herein showing that for example, Na prefers the A1-site, K is fully disordered over both A1- and A2- sites, and Rb has a preference for A2-site occupation. From 100 % to 0 % R on A1-site occupation, there is also a general decrease in tetragonality, likely influencing the T_C via modification of the B-site environment. The influence of A-site disorder on the B-site can be alluded to through Nb-O-Nb angles in the c-direction
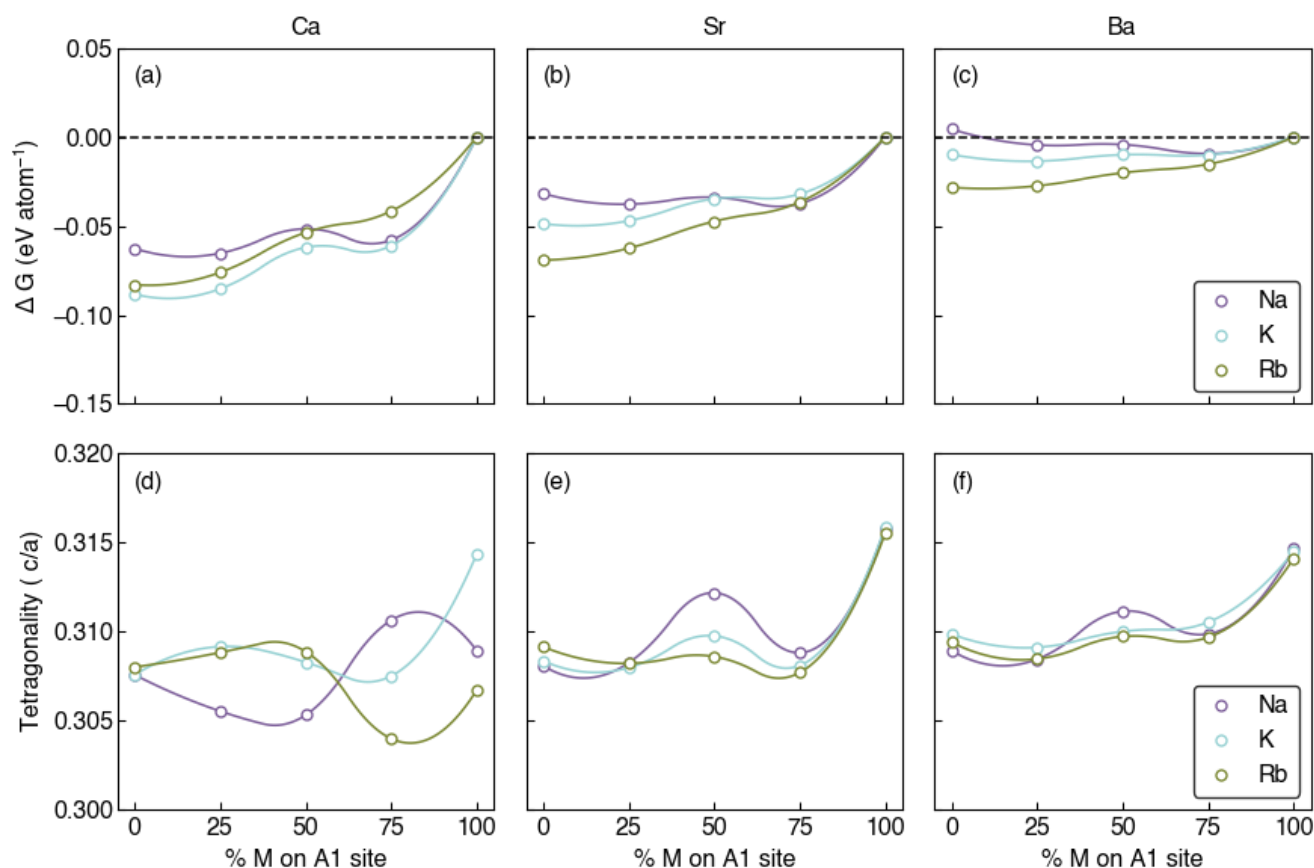
Figure 11. The thermodynamics of cation site disorder as a function of R (Ca, Sr, Ba) and M cation (Na, K, Rb). In the top row (a,b,c) the Gibbs free energy of configuration is shown relative to the ordered state, the second row (d,e,f) shows the probabilistically averaged tetragonality

and antibonding character of the Nb-O (Figure S22 and Table S8 in SI). Deviation from the fully ordered TTB composition is accompanied by a decrease in the Nb-O-Nb angle from ~178 ° to ~170° for all Ba-compositions showing that some octahedral tilting will be expected. In addition to this, there is minimal deviation in the antibonding nature in the NbO_6 octahedral framework both between M-compositions as well as with A-site interchange.

For the Sr-based compositions, it is shown that for Na and K, more A-site disorder is expected, with Rb strongly preferring the A2-site owing to its much larger radii than Sr. As Ca's ionic radii is smaller than those of Na, K, or Rb; Ca sits primarily on the A1-site. Experimentally $Ca_2KNb_5O_{15}$[45] exists in the TTB structure with tetragonal symmetry, while $Ca_2NaNb_5O_{15}$ adopts an orthorhombic space group[49]. In general, the tetragonality is very similar between Ba, Sr, and Ca initially dropping off from the 100 % R on A1-site converging around 0.307 upon A-site disorder.

Discussion

Evolution of crystal structure with M

A decrease in the M-cation size is associated with a decrease in the lattice parameters of all the studied Ba-based TTB compounds, in line with expectations. This is clearly demonstrated in Figure 12 where the lattice parameters are plotted as a function of the ionic radius of the M-cation. A close to linear relation is observed between the M-cation size and the in-plane a-parameters. The in-plane dimensions of the unit cell of the TTB are to a large degree determined by the size of the cations located at the A-sites. For the out-of-plane c-parameter, the correlation is not as pronounced and particularly the drop
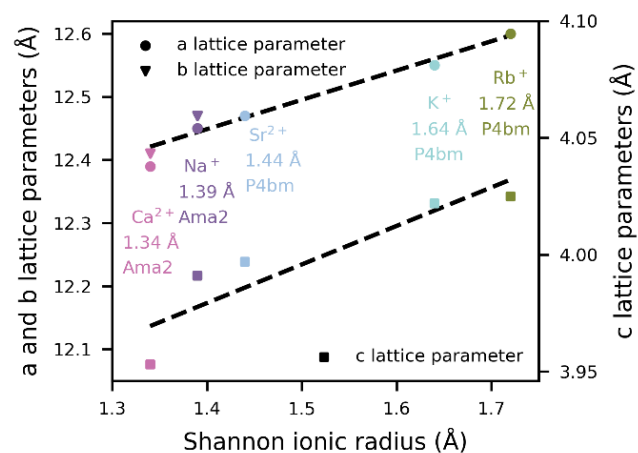

Figure 12. Lattice parameter evolution with size of M-cation in the BMN and BMNT series. A decrease in the M-cation size is associated with a decrease in the lattice parameters of all the studied TTB-compounds

observed for the c-parameter of BCNT deviate from the trend. Besides the size of the A and B cations, the magnitude of the polarisation will also affect the c-parameter since the polarisation is oriented along this crystallographic direction.

A shift from tetragonal to orthorhombic symmetry takes place as the M-cation becomes smaller. We hypothesise that the average size of the cations occupying the A1-sites decides whether the structure becomes tetragonal or orthorhombic. The average size of the cations occupying the A1-site is determined by the size of the respective M-cations as well as the degree of cation disorder. Orthorhombic BNN and BCNT are composed of small M-cations and large degree of ordering. Considering the occupation of both M and Ba on the A1-site, the average size of cations occupying the A1-site is 1.42 and 1.36 Å and in BNN and BCNT, respectively. For BSNT, which is tetragonal, the average size is 1.48 Å.

In the solid solution series $(Ba, Sr)_6 Nb_8Ti_2O_{30}$, a shift from tetragonal to orthorhombic symmetry takes place at about 0.2-0.3 Ba-content.[12, 50] So, an orthorhombic symmetry is realised as the A-site average ionic radius is reduced with increasing Sr-content. Yet, tetragonal $Sr_4Ba_2Ti_2Nb_8O_{30}$ has A-cations with smaller average ionic radii than orthorhombic BCNT, meaning that the mean size of the A-cations is not sufficient to rationalise whether tetragonal or orthorhombic structure is exhibited. Alternatively, the Ba-occupation on the A1 position is likely to be reduced as the overall Ba-content is lowered, leading to a shift into the orthorhombic structure as the average ionic A1-size is sufficiently reduced with increasing Sr-content. When all A1-sites are occupied by Sr, as in $Sr_6 Nb_8Ti_2O_{30}$ (SNT), the average ionic A1-site radius is 1.44 Å and this is too small to stabilise the tetragonal structure. Thus, the tetragonal symmetry is stabilised by cation disorder in BSNT, resulting in Ba-cations on the A1-site and an increase in the average ionic size at the A1-site.

The crystal structure of SNT is orthorhombic with space group $Pna2_1$ resulting from polar distortion Γ_3^- and Z_5^+(P3) octahedral tilting.[50] The instability found in SNT was also identified by first principles calculations[10] in $SrNb_2O_6$, while this instability was not found for $BaNb_2O_6$. All the A-sites are filled with Sr in SNT, which means that a specific size difference between A1- and A2-cations is not required to stabilize the orthorhombic crystal structure.

In ABO_3 perovskites, which has a similar A1-site, small A-cations are known to induce octahedral tilting, which is associated with a lowering of the symmetry.[51] The octahedral tilting in perovskites reduces the A-O distance, while maintaining the octahedra nearly undistorted. The similarity between the crystal structures of perovskites and TTBs suggests that the reduction from tetragonal to orthorhombic symmetry observed for filled Ba-based TTBs is related to a reduced size of the A1-cation. Lin et al. describe how the filled Pb-based TTBs $Pb_2RNb_5O_{15}$ (R = Rb, K, Pb, Ag, $K_{0.5}Li_{0.5}$, Na), experience doubling of the c-parameter induced by octahedral tilting for small R-cations.[52] The authors suggest that tilting of the NbO_6 octahedra can balance a negative pressure that is formed for the A-site tunnels which are filled by small R-cations. For this to be the valid cause of the orthorhombic symmetry observed in BNN and

BCNT, the orthorhombic space group needs to facilitate octahedral tilting.[43]

For BNN, it has been an ongoing discussion related to what is the true room temperature space group. The $Ama2$ space group, first suggested by Labbe et al.[53], has recently been confirmed most probable based on group theory and thorough literature review by Whittle et al.[54], as well as by Grendal et al.[19] through their experimental work. Grendal and co-workers also demonstrate how tilting occurs with the ferroelastic transition and is not allowed at temperatures above said orthorhombic distortion. BCNT is reported by Neurgaonkar et al.[12] as $Cmm2$, however as we expect octahedral tilting, the $Ama2$ space group , which facilitate octahedral tilts, was ultimately reported. However, Rietveld refinement using $Cmm2$ (Table S3 in SI) was conducted, and the lattice parameters and occupation reported experience only very slight variation between the two refinements.

The orthorhombic to tetragonal phase transition of BNN does not affect the dielectric constant noticeably, only a minor feature is observed in the loss data (Figure S2 (c) in SI) at the temperature where the ferroelastic transition is expected. A corresponding transition is inferred for BCNT, but the transition temperature cannot be determined based on the dielectric data (Figure S5). The ferroelastic phase transition for BNN was reported to be a second order phase transition with no discontinued change in volume or enthalpy[42]. Supported by first principles calculations it was concluded that the orthorhombic to tetragonal phase transition, and thereby the orthorhombic distortion of the crystal lattice did not have a pronounced influence on the polarization and the ferroelectric phase transition temperature.

Cation disorder

In the TTB crystal structure, there is an overall cation disorder associated with how many cation species that are involved. Increasing number of cations gives a higher overall cation disorder and therefore the BMNT-series have a higher overall cation disorder than the BMN-series as they have 4 and 3 cationic species, respectively. The possible overall cation disorder within each series is the same. Even though the compositions within a series have the same overall cation disorder, A site-specific disorder is associated with how the respective A- and B-cations are distributed across the A- and B-subsites.

The observed cation occupancy for M on the A1 site is plotted as a function of the Shannon ionic radii in Figure 13. The occupancy correlates well with the ionic size of M. In general, larger A-cations have a preference to occupy the larger A2-sites, while smaller A-cations prefer to be located at the smaller A1-sites. But cross occupation, which is governed by the cation size difference, also takes place. This cross occupation leads to occupational disorder on the A1 and A2 sites. The level of disorder on each site is highest if the occupation of both species is 0.5, while the overall configurational entropy for a TTB with this stoichiometry is highest when M occupation on A1 site is 0.4[7].
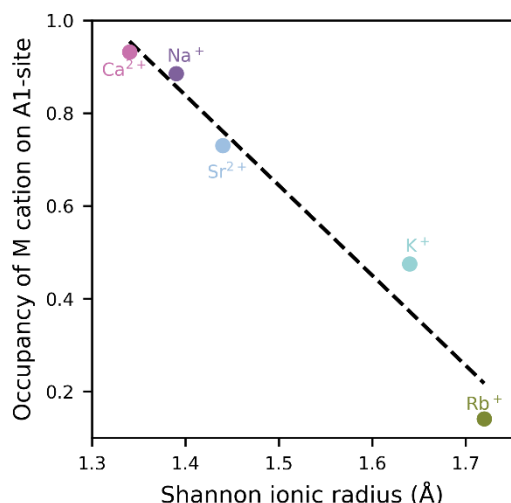
Figure 13. Occupancy of M-cation on the A1-site in BMN and BMNT TTBs as a function of the Shannon ionic radii of the respective M-cation.

In this study the cation size difference, defined as dR = rBa - rM, and ultimately the level of cross occupation can be discussed with respect to the M-cation size. The distribution of cations on the two A-sites in BCNT and BSNT is found to be consistent with what is previously reported for BNN, BKN and BRN, in terms of larger M-cations leading to a lower occupancy of M-cations on the A1-site due to cross occupation of Ba and M on the two A-subsites[7]. The A-site cross occupation observed in BSNT contrasts with previous report by Whittle and Schmid[50] but is in good agreement with a recent XPS study[55].

The thermodynamics calculations by DFT also indicate a drive for cation disorder in all three BMN compounds. Figure 11 (c) demonstrates how it is energetically favourable (more negative ΔG) for all three BMN materials to deviate from the 100 % M on A1-site. With increasing size of the M-cation, a preference for higher cation cross occupation follows, in line with reported experimental work.[7]

Correlation of T_C with the size of M

T_C of the filled Ba-based TTBs decreases with increasing size of M-cation within both the BMN and the BMNT series. The linear dependence of T_C with the M-size is also completely in line with what is observed in the $Ba_4M_2Nb_6Ti_4O_{30}$ (BM3NT, M= Bi^{3+}, La^{3+}, Nd^{3+}, Sm^{3+}, Gd^{3+}) series studied by Stenntett *and co-workers*[56]. This is shown in Figure 14. From quenching experiments, it is known that cation disorder influences the T_C of TTBs[6, 9]. Thus, the observed drop in T_C with increasing M-cation size can be correlated with the increased disorder related to the larger M-cations in BMN and BMNT TTBs. But all the M-cations in the BM3NT series are small, meaning that the dR is large. This give little or no expectation of cross occupation of Ba and M between the A1 and A2 sites, and agrees with results for BL3NT [56]. Therefore, cation disorder on the A-sites cannot explain the decrease in T_C alone. The T_C in the BM3NT series is proposed to be governed primarily by dR, and ultimately the size of the M-cation that occupies the A1-site. Morrison *et al.*[57] argue that

occupation of smaller cations in the square A1-sites activates B2-cation displacement stabilising the dipole moment within the structure and therefore raising the transition temperature in TTBs. However, a significant drop in T_C is observed with the introduction of Ti on the B-sites in BMNT and BM3NT, which also is associated with increase in the level of disorder in the TTB-system. Comparing BNN, BCNT and BL3NT, which have M-cations of comparable size, the pure niobate compound BNN has T_C of 250 and 530 °C higher than the compound with 20 and 40 % Ti on the B-site, respectively.

As A-site disorder plays a significant role in the BMN series, T_C should also be discussed with respect to the mean size of the cations occupying the A1-site rather than M-cation size alone. However, the mean size of the cations occupying the A1-site is virtually the same in BRN (1.6254 Å) and BKN (1.6250 Å). If only taking A1-size into account T_C should be similar in these two compounds, but this is not the case. In the fully ordered systems, M-cation size is a direct measure of dR, but in systems with cation disorder the effective size difference should be considered as the difference between the mean size of cations occupying the A2 and A1 sites, individually. In this case BRN has a larger effective dR than BKN, meaning that the T_C of BRN should be larger than BKN, which is not the case. Overall cation disorder also fails to explain why BRN has the lowest observed T_C in the BMN series even though the configurational entropy suggests that BKN is more disordered. However, the disorder is larger for BRN with respect for the A2-sites, raising the question of whether the TTB structure is more sensitive to mixed occupation on the A2-site, with respect to T_C.

Tetragonality is often discussed with respect to T_C in TTBs. Morrison et al. report that a lowering of the T_C is associated with a drop in the tetragonality[11, 58]. In Figure 15, the tetragonality of BMN and BMNT TTBs are plotted as function of the size of their respective M-cations. Tetragonality values for the BMN-series retrieved from both the non-polar aristotype *P4/mbm* and the
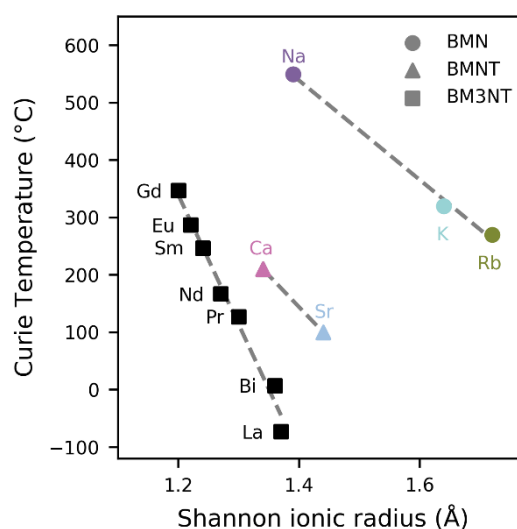

Figure 14. Curie temperature of TTBs as function of the Shannon ionic radii of their respective M-cation. The datapoints plotted with square markers are retrieved from ref. 55.
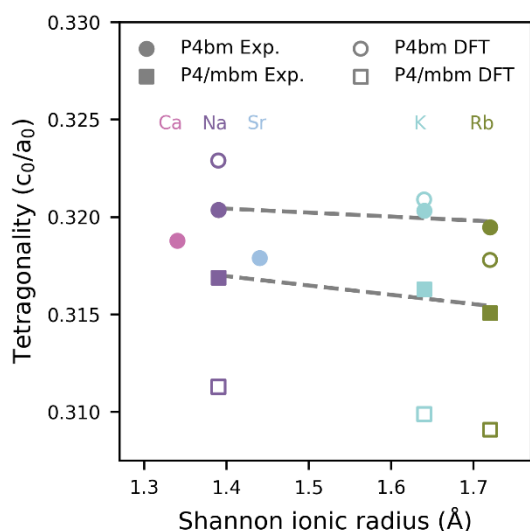
Figure 15. Tetragonality of BMN and BMNT TTBs as function of the Shannon ionic radii of their respective M-cations. Tetragonality values are calculated from lattice parameters retrieved from Rietveld refinement of XRD measured at ambient (filled circle) and non-ambient (filled square) temperature as well as from lattice parameters retrieved from DFT calculations (empty circles and squares). The presented tetragonality data from DFT is taken from structures with A-site occupation corresponding to the occupation observed from Rietveld refinement on the specific compound. Linear trendlines are plotted for the XRD retrieved values of the BMN-series. The average of a_0 and b_0 is used to calculate the tetragonality for BNN and BCNT. The non-ambient tetragonality for BNN is calculated from lattice parameter values in ref. 41.

polar $P4bm$/Ama2 space group from Rietveld refinement of XRD at ambient and non-ambient temperature as well as from DFT calculations, are included. For BCNT and BSNT, only the tetragonality calculated from refinement of ambient temperature XRD is included. All four datasets show a slight decrease in the tetragonality with increasing size of the M-cation. The additional drop in T_C, for BCNT and BSNT, suggested assigned to the introduction of Ti on B-sites, is also mirrored in the tetragonality. The values calculated using parameters from the DFT calculations have a larger difference between the P4bm and $P4$/mbm symmetry than observed between the ambient and non-ambient temperature structures retrieved from XRD refinements. It is important to note, that whilst the probable structures are locked in at 1000 K, the lattice parameters are represented by 0 K relaxations thus discrepancies are expected between experiment and calculation.

DFT calculations were performed on stoichiometrically "perfect" TTB compositions, where R and M-cations are defined to stay on the A2- and A1-sites, respectively. Based on the relative ΔE values presented in Figure 10 (c), an increase in T_C is expected with both increasing M and R radii. The dependence of T_C with R-cation size agrees well with reported experimental work[21, 45, 46], while the dependence of T_C with M-cation size, reported here, actually show the opposite of what the DFT calculations suggest, namely that the highest T_C is expected for BRN. The large deviation from experimental results indicates that the T_C of the TTB compounds is heavily influenced by disorder and deviations from the stoichiometric perfectly ordered TTB structure. No real change is observed in the

antibonding nature of the Nb-O with composition or cross occupation within the A-sites.

Dielectric properties in relation to size of M

There is no evidence of diffusive or relaxor-like behaviour in the filled and single B-cation BMN TTBs, despite some having a small dR and a large degree of cation disorder. More diffusive dielectric behaviour with decreasing dR is, however, reported for a range of different TTB series with Ti introduced as a second B-site cation, such as for example BM3TN[56], ($Sr_{1-x}Ba_x$)$Nd_2Ti_4Nb_6O_{30}$ and $Sr_4(La_{1-x}Sm_x)_2Ti_4Nb_6O_{30}$[16]. Diffuse ferroelectric to paraelectric transitions are also reported for the two Ti-containing TTBs $Ba_3TiNb_5O_{15}$ (BTN) and $Sr_3TiNb_5O_{15}$ (STN)[15, 59]. In these two compounds, dR = 0.

BSNT is effectively a 4:2 BTN-STN solid solution and the frequency dispersion observed is therefore expected, despite previous reports of it having little relaxor characteristic[60]. For STN and BTN the ferroelectric phase transition is reported at 100-150 °C and 150-200 °C, respectively[12, 15, 59]. For BSNT the peak permittivity is located at ~ 100 °C (Figure S7(a) in SI), before the dispersion spreads out in a wider temperature range. A second relaxation is reported at ~ 300 °C for both STN, BTN and the related composition $Ba_3ZrNb_5O_{15}$ (BZN) by Shi et al.[59], similar to what is observed for BSNT before the wide dispersion fully develops. They suggest that this peak can be related to motion of charge carriers, dynamics of polar nano-regions or space charge effects. The frequency dispersion observed for the ferroelectric transition in BTN and STN can be related to the B-site disorder and is also expected in BSNT. However, upon thermal cycling the frequency dispersion observed is extreme. This together with the clear maxima in the permittivity observed at about 300 °C before the wide dispersion fully develops, suggest that the wide frequency dispersion observed is caused by several overlapping and frequency dispersed relaxations.

For BCNT no frequency dispersion is seen in the ferroelectric transition, but a second relaxation is also observed for BCNT around 300 °C. Additionally, relaxor properties are present at larger dR for the BM3TN series, which have higher B-site mixing than the BMNT compounds. For the BM3TN compounds relaxor properties are reported for dR of 0.26, while in BCNT and BNN that have similar dR diffusive to normal ferroelectric behaviour is present.

Ferroelectric properties

All five compounds show weak maximum and remnant polarizations and none of them exhibited well saturated (squared) P-E-loops at the maximum applied field strength. One explanation for this could be that the materials exhibit hard ferroelectric behaviour, that is, that the domain switching is pinned by charged defects and requires large fields before the P-E loops will open. Both the P-E- and S-E-loops are reminiscent of those reported for the hard ferroelectric PZT by Viola et al.[61]. However, even the application of electric fields at elevated temperatures (Figure S15-S17 in SI) did not appear to improve the degree of domain switching. Thus, it is also possible that the

dielectric breakdown fields were too low for saturated switching behaviour to be able to manifest, which could suggest that higher densities, than achieved here, are required to apply high enough fields to achieve full saturation without dielectric breakdown. P-E-loops have also previously been reported for both BNN [62, 63] and BKN [64] but, to our best knowledge, not for BRN, BCNT and BSNT.

Similar unsaturated P-E-loops with small remnant and saturated polarizations have been reported for other TTB compositions, indicating that this is a common feature among the TTB ferroelectrics[15, 57]. The fact that the TTBs are uniaxial ferroelectrics, also suggests that the coercive fields may be large and the P-E and S-E loops have no contributions from ferroelastic domain switching. It also tells us that texturing is critical for achieving high macroscopic polarization and strain responses in polycrystalline ceramics. For example, for BKN ceramics maximum polarizations of 4 and 5.5 $\mu C/cm^2$ were achieved at fields of 70 kV/cm for textures consisting of the c-axis being mostly perpendicular or parallel to the applied field, respectively.[64] A higher degree of texturing increases the degree of saturation, "square-ness", exhibited by the PE-loop, with P_r of 1.3 and 2.9 $\mu C/cm^2$, for perpendicular or parallel configuration, respectively. P-E-loops of ceramic BNN with maximum polarisation of 8 $\mu C/cm^2$ and P_r of about 1.5 $\mu C/cm^2$ at fields of 150 kV/cm were reported by Li et al.[63], while for BNN thin films, with a high degree of texturing, maximum polarizations of 15 $\mu C/cm^2$ and P_r of 12.3 $\mu C/cm^2$ at 200 kV/cm was reported by Yogo et al.[62] The loop reported by Yogo et al. has been used to exemplify how a fully saturated PE-loop should look.[65]

The weak polarization and unsaturated loops are most likely the result of a "diluted" polarization response caused by the random distribution of polarization directions, that is the c-axis, throughout the untextured microstructures. As the ceramics are only uniaxial ferroelectrics there is a limited amount of polarization alignment that is possible when the crystal structure of each grain is randomly oriented.

Conclusions

Dense and phase pure BMN and BMNT ceramics were prepared by a two-step solid state synthesis route. A close to linear relation between the in-plane lattice parameter and the size of the M-cation was observed, as expected. The crystal symmetry of BCNT and BNN, which are the two compounds with the smallest M-cation size, was found to be orthorhombic, while BKN, BRN and BSNT, with the larger M-cation were observed to have a tetragonal symmetry. The average size of the cations occupying the A1-site was proposed to be the main factor influencing the symmetry, similar to observed for perovskites. $Ba_4M_2Nb_8Ti_2O_{30}$ was shown to possess cation disorder on the A-sites in line with previous work on $Ba_4M_2Nb_{10}O_{30}$. Non-ambient temperature X-ray diffraction exposed that contraction of the in-plane (a), and expansion of the out-of-plane (c) lattice parameters take place at the ferroelectric phase transition for $Ba_4M_2Nb_{10}O_{30}$. T_C decrease systematically with increasing size of the M-cation within both compositional series. The drop in T_C

is apparently related to both A-site cation disorder and the size difference dR separately, even though the two are closely linked. Additionally, the T_C decreased with introduction of Ti as a second B-site cation. The observed relation between T_C and composition is mirrored in the tetragonality. Normal ferroelectric behaviour is implied for the BMN series by the character of dielectric spectroscopy data, as well as PE-loops for BNN and BKN. Wide frequency dispersion was observed in the dielectric spectroscopy data for BSNT. A second frequency dispersed relaxation above the ferroelectric transition was present for both for BCNT and BSNT.

Author Contributions

NSL have conducted the experimental work, supervised by TG, MAE and JW. BADW conducted the computational work. NSL wrote the first draft to the manuscript with contributions from BADW and TG. All authors contributed to the review and editing of the final manuscript and have given approval to the final version of the manuscript.

Conflicts of interest

There are no conflicts to declare.

Acknowledgements

Notes and references

1. G. H. Haertling, *J Am Ceram Soc*, 1999, **82**, 797-818.
2. M. E. Lines and A. M. Glass, *Principles and Applications of Ferroelectrics and Related Materials* Oxford University Press, 1977.
3. A. Simon and J. Ravez, *Cr Chim*, 2006, **9**, 1268-1276.
4. X. Zhu, M. Fu, M. C. Stennett, P. M. Vilarinho, I. Levin, C. A. Randall, J. Gardner, F. D. Morrison and I. M. Reaney, *Chem Mater*, 2015, **27**, 3250-3261.
5. J. Ravez, A. Perron, J. P. Chaminad, P. Hagenmuller and L. Rivoallan, *J Solid State Chem*, 1974, **10**, 274-281.
6. S. S. Aamlid, S. M. Selbach and T. Grande, *Materials*, 2019, **12**.
7. I.-E. Nylund, N. S. Løndal, J. Walker, P. E. Vullum, M.-A. Einarsrud and T. Grande, *Inorg Chem*, 2022, **61**, 15540-15546.
8. J. Ravez, A. Perron-Simon and P. Hagenmuller, *Ann Chim France*, 1976, **1**, 251-268.
9. G. Burns and D. F. Okane, *Phys Lett A*, 1969, **A 28**, 776-&.
10. G. H. Olsen, U. Aschauer, N. A. Spaldin, S. M. Selbach and T. Grande, *Phys Rev B*, 2016, **93**.
11. D. C. Arnold and F. D. Morrison, *J Mater Chem*, 2009, **19**, 6485-6488.

12. R. R. Neurgaonkar, J. G. Nelson and J. R. Oliver, *Mater Res Bull*, 1992, **27**, 677-684.
13. E. O. Chi, A. Gandini, K. M. Ok, Z. Lei and P. S. Halasyamani, *Chem Mater*, 2004, **16**, 3616-3622.
14. V. V. Shvartsman and D. C. Lupascu, *J Am Ceram Soc*, 2012, **95**, 1-26.
15. Y. Yuan, X. M. Chen and Y. J. Wu, *J Appl Phys*, 2005, **98**.
16. X. L. Zhu, K. Li and X. M. Chen, *J Am Ceram Soc*, 2014, **97**, 329-338.
17. G. A. Smolenskii, V. A. Isupov, A. I. Agranovskaya and S. N. Popov, *Sov Phys-Sol State*, 1961, **2**, 2584-2594.
18. G. H. Olsen, M. H. Sorby, S. M. Selbach and T. Grande, *Chem Mater*, 2017, **29**, 6414-6424.
19. O. G. Grendal, D. M. Evans and S. S. Aamlid, *Journal of Applied Crystallography* 2023, **56**, 1456-1465.
20. J. G. Carrio, Y. P. Mascarenhas, W. Yelon, I. A. Santos, D. Garcia and J. A. Eiras, *Material Research* 2002, 57-62.
21. E. A. Giess, B. A. Scott, G. Burns, D. F. Okane and A. Segmuller, *J Am Ceram Soc*, 1969, **52**, 276-281.
22. G. Kresse and J. Furthmuller, *Phys Rev B*, 1996, **54**, 11169-11186.
23. G. Kresse and J. Furthmuller, *Comp Mater Sci*, 1996, **6**, 15-50.
24. G. Kresse and J. Hafner, *Phys Rev B*, 1994, **49**, 14251-14269.
25. G. Kresse and J. Hafner, *Phys Rev B*, 1993, **47**, 558.
26. P. E. Blöchl, *Phys Rev B*, 1994, **50**, 17953–17979.
27. J. P. Perdew, K. Burke and M. Ernzerhof, *Phys Rev Lett*, 1996, **77**, 3865-3868.
28. J. P. Perdew, A. Ruzsinszky, G. I. Csonka, O. A. Vydrov, G. E. Scuseria, L. A. Constantin, X. L. Zhou and K. Burke, *Phys Rev Lett*, 2008, **100**.
29. A. M. Ganose and D. O. Scanlon, *J Mater Chem C*, 2016, **4**, 1467-1475.
30. B. A. D. Williamson, G. J. Limburn, G. W. Watson, G. Hyett and D. O. Scanlon, *Matter-Us*, 2020, **3**, 759-781.
31. A. Togo and I. Tanaka, *Scripta Mater*, 2015, **108**, 1-5.
32. A. M. Ganose, A. J. Jackson and D. O. Scanlon, *Journal of Open Source Software*, 2018, **3**, 717.
33. J. M. Skelton, L. A. Burton, S. C. Parker, A. Walsh, C. E. Kim, A. Soon, J. Buckeridge, A. A. Sokol, C. R. A. Catlow, A. Togo and I. Tanaka, *Phys Rev Lett*, 2016, **117**.
34. W. Rahim, J. M. Skelton, C. N. Savory, I. R. Evans, J. S. O. Evans, A. Walsh and D. O. Scanlon, *Chem Sci*, 2020, **11**, 7904-7909.
35. R. Grau-Crespo, S. Hamad, C. R. A. Catlow and N. H. de Leeuw, *J Phys-Condens Mat*, 2007, **19**.
36. B. J. Morgan, *Journal of Open Source Software*, 2017, **2**, 370.
37. S. Benny, R. Grau-Crespo and N. H. de Leeuw, *Phys Chem Chem Phys*, 2009, **11**, 808-815.
38. R. Dronskowski and P. E. Blochl, *J Phys Chem-Us*, 1993, **97**, 8617-8624.
39. J. George, G. Petretto, A. Naik, M. Esters, A. J. Jackson, R. Nelson, R. Dronskowski, G. M. Rignanese and G. Hautier, *Chempluschem*, 2022, **87**.
40. S. P. Ong, W. D. Richards, A. Jain, G. Hautier, M. Kocher, S. Cholia, D. Gunter, V. L. Chevrier, K. A. Persson and G. Ceder, *Comp Mater Sci*, 2013, **68**, 314-319.
41. D. Waroquiers, J. George, M. Horton, S. Schenk, K. A. Persson, G. M. Rignanese, X. Gonze and G. Hautier, *Acta Crystallographica, Section B: Structural Science, Crystal Engineering and Materials*, 2020, **76**, 683-695.
42. S. S. Aamlid, S. M. Selbach and T. Grande, *Inorg Chem*, 2020, **59**, 8514-8521.
43. T. A. Whittle, C. J. Howard and S. Schmid, *Acta Crystallographica, Section B: Structural Science, Crystal Engineering and Materials*, 2021, **77**, 981-985.
44. R. D. Shannon, *Acta Crystallogr A*, 1976, **32**, 751-767.
45. B. Behera, P. Nayak and R. N. P. Choudhary, *Cent Eur J Phys*, 2008, **6**, 289-295.
46. S. I. Hamazaki, S. Sawada, S. Kojima, M. Tsukioka and M. Takashige, *J Phys Soc Jpn*, 1995, **64**, 4004-4012.
47. P. Goudochnikov and A. J. Bell, *J Phys-Condens Mat*, 2007, **19**.
48. I. Pallikara, P. Kayastha, J. M. Skelton and L. D. Whalley, *Electron Struct*, 2022, **4**.
49. B. Behera, P. Nayak and R. N. P. Choudhary, *Mod Phys Lett B*, 2009, **23**, 97-109.
50. T. A. Whittle and S. Schmid, *Powder Diffr*, 2014, **29**, S15-S18.
51. P. M. Woodward, *Acta Crystallogr B*, 1997, **53**, 32-43.
52. K. Lin, L. You, Q. Li, J. Chen, J. X. Deng and X. R. Xing, *Inorg Chem*, 2016, **55**, 8130-8139.
53. P. Labbe, H. Leligny, B. Raveau, J. Schneck and J. C. Toledano, *J Phys-Condens Mat*, 1990, **2**, 25-43.
54. T. A. Whittle, S. Schmid and C. J. Howard, *Acta Crystallographica, Section B: Structural Science, Crystal Engineering and Materials*, 2015, **71**, 342-348.
55. D. Jiang, PhD, University of Manchester, 2019.
56. M. C. Stennett, I. M. Reaney, G. C. Miles, D. I. Woodward, A. R. West, C. A. Kirk and I. Levin, *J Appl Phys*, 2007, **101**.
57. A. Rotaru, A. J. Miller, D. C. Arnold and F. D. Morrison, *Philos T R Soc A*, 2014, **372**.
58. J. Gardner and F. D. Morrison, *Dalton T*, 2014, **43**, 11687-11695.
59. X. Shi and N. H. Khansur, *Crystals*, 2023, **13**.
60. R. R. Neurgaonkar, *Photorefractive tungsten bronze crystals for optical computing*, Rockwell International Science Center, 1993.
61. G. Viola, T. Saunders, X. Wei, K. B. Chong, H. Luo, M. J. Reece and H. Yan, *Journal of Advanced Dielectrics*, 2013, **3**.
62. T. Yogo, W. Sakamoto, T. Isaji, M. Ichida, A. Nakamura and S. Hirano, *J Am Ceram Soc*, 1999, **82**, 2672-2676.
63. R. Li, Y. P. Pu, Q. W. Zhang, W. Wang, J. W. Li, X. Y. Du, M. Chen, X. Zhang and Z. X. Sun, *J Eur Ceram Soc*, 2020, **40**, 4509-4516.
64. K. Kakimoto, T. Yoshifuji and H. Ohsato, *Jpn J Appl Phys 1*, 2006, **45**, 7435-7439.
65. J. F. Scott, *J Phys-Condens Mat*, 2008, **20**.